PCCP

Cite this: *Phys. Chem. Chem. Phys.*, 2011, **13**, 17870–17884

www.rsc.org/pccp

**PAPER**

# On the chemical processing of hydrocarbon surfaces by fast oxygen ions†

**Courtney Ennis,[a] Hanqiu Yuan,[b] S. J. Sibener[b] and Ralf I. Kaiser[a]**

***Received 3rd June 2011, Accepted 22nd August 2011***
**DOI: 10.1039/c1cp21800j**



Solid methane ($CH_4$), ethane ($C_2H_6$), and ethylene ($C_2H_4$) ices (thickness: 120 ± 40 nm; 10 K), as well as high-density polyethylene (HDPE: $[C_2H_4]_n$) films (thickness: 130 ± 20 nm; 10, 100, and 300 K), were irradiated with mono-energetic oxygen ions ($\Phi \sim 6 \times 10^{15}$ cm$^{-2}$) of a kinetic energy of 5 keV to simulate the exposure of Solar System hydrocarbon ices and aerospace polymers to oxygen ions sourced from the solar wind and planetary magnetospheres. On-line Fourier-transform infrared spectroscopy (FTIR) was used to identify the following $O^+$ induced reaction pathways in the solid-state: (i) ethane formation from methane ice *via* recombination of methyl ($CH_3$) radicals, (ii) ethane conversion back to methane *via* methylene ($CH_2$) retro-insertion, (iii) ethane decomposing to acetylene *via* ethylene through successive hydrogen elimination steps, and (iv) ethylene conversion to acetylene *via* hydrogen elimination. No changes were observed in the irradiated PE samples *via* infrared spectroscopy. In addition, mass spectrometry detected small abundances of methanol ($CH_3OH$) sublimed from the irradiated methane and ethane condensates during controlled heating. The detection of methanol suggests an implantation and neutralization of the oxygen ions within the surface where atomic oxygen (O) then undergoes insertion into a C–H bond of methane. Atomic hydrogen (H) recombination in forming molecular hydrogen and recombination of implanted oxygen atoms to molecular oxygen ($O_2$) are also inferred to proceed at high cross-sections. A comparison of the reaction rates and product yields to those obtained from experiments involving 5 keV electrons, suggests that the chemical alteration of the hydrocarbon ice samples is driven primarily by electronic stopping interactions and to a lesser extent by nuclear interactions.

## 1. Introduction

Condensed hydrocarbon ices have been observed on the surfaces of planets and their moons in the outer Solar System.[1,2] The Cassini-Huygens mission to Saturn's largest moon Titan exposed a surface composition rich in ethane ($C_2H_6$)—a primary constituent of Titan's polar 'lake' features—[3] and hydrocarbon precipitates ($C_xH_y$ $x \geq y > 2$) produced by radiolytic processes on the surface and/or in the atmosphere.[4,5] In addition to Titan, Enceladus, for instance, displays a methane abundance of 1.6 ± 0.4% within its plume of subsurface material.[6] Looking beyond the Saturnian system into the icy realm of Trans Neptunian Objects (TNOs—including Pluto, Charon, Triton, and Kuiper Belt Objects (KBOs))—hydrocarbons have also been detected on their surfaces. These organics are either dissolved within a frozen molecular nitrogen ($N_2$) matrix (Triton,[7] Pluto,[8,9] Quaoar,[10] KBO-2005-FY9[11]) or are present as pure methane ice (Pluto[9]). For Pluto[12] and Triton,[13] theoretical models predict that the volatile surface methane sublimes. Atmospheric photochemical processes are expected to form ethane ($C_2H_6$), acetylene ($C_2H_2$), and ethylene ($C_2H_4$); these heavier molecules can then precipitate and re-condense onto the frozen surfaces (35–50 K). Finally, spectroscopic observation of the icy corona surrounding long period cometary objects (C/1996 B2 Hyakutake[14,15] and C/1995 O1 Hale-Bopp[16]) detected methane, ethane, and acetylene ranging from 0.1–1% relative abundance to water; these organics sublime from their surfaces once the comets approach warmer regions of the Solar System.

The planetary surface hydrocarbons are continually exposed to energetic particles. Galactic cosmic rays (GCRs)[17]—comprising of about 87% protons ($p$, $H^+$) and 12% helium nuclei (α-particles, $He^{2+}$)—as well as UV photons ($\lambda < 13.6$ eV; $\Phi = 10^3$ photons cm$^{-2}$ s$^{-1}$) and a few heavier nuclei such as $O^+$—are a significant source of energetic ($E_k > 0.1$ GeV) particles in the outer Solar System. The lower energy component of GCR also plays a significant role in the chemical processing of KBOs.[18] Within the inner Solar System environment, the solar wind (96% $H^+$, 4% $He^{2+}$, $<10^{-3}$ heavy ions: ~1 keV per amu, and UV photons) results in a higher energy deposition within these ices. Charged

[a] *Department of Chemistry, University of Hawai'i at Manoa, Honolulu, HI 96822, USA*
[b] *The James Frank Institute and Department of Chemistry, The University of Chicago, 929 East 57th Street, Chicago, IL 60637*
† $O^+$ Irradiation of Hydrocarbons.

particles can also be trapped within the magnetospheres of the planets such as Jupiter and Saturn as well as Earth. Here, oxygen-bearing molecules like water, which presents the dominating component of Solar System ices, are constantly exposed to ionizing radiation.[19–21] Besides protons, these processes lead to the formation of energetic oxygen atoms and ions ($O^+$).[22,23] These oxygen ions may then be accumulated in magnetospheres (*e.g.* Saturn[22]), where they are accelerated to kinetic energies of up to a few keV. Therefore, as a satellite body orbits within the magnetosphere, oxygen ions can then collide with the icy surfaces to generate new oxygen-bearing chemical products. Furthermore, these new molecules may act as potential reactants in the formation of higher-order species of biological importance.

Despite the prevalence of oxygen ion reactions, there have only been a small number of experimental investigations into the radiolytic processing of Solar System surfaces by energetic oxygen ions sourced from magnetospheric ions. Gomis *et al.*[24] studied the effects of 30 keV $O^+$ ions ($7 \times 10^{15}$ ions $cm^{-2}$) on low temperature (15 and 77 K) water ice samples ($\sim$0.5 μm) monitoring the temporal increase in hydrogen peroxide ($H_2O_2$) *via* Fourier transform infrared (FTIR) spectroscopy. A similar study[25] irradiated silicon samples with 30 keV $O^+$ ions yielded mid-IR absorption bands associated with silica (Si–O) bond formation. Other early experiments[26] implanted 15 keV $O^+$ ions ($7 \times 10^{15}$ ions $cm^{-2}$) into methane ice targets hoping to observe carbon monoxide (CO) and carbon dioxide ($CO_2$) as irradiation products. However, these species were not observed—as otherwise detected in other carbonaceous ice samples exposed to $H^+$ and $He^+$ ions. In addition, there have been a number of laboratory studies as summarized in Ennis & Kaiser[27] involving the exposure of polyethylene (PE: $[C_2H_4]_n$) films with an array of energetic particles, primarily to test the degradation resistance of the polymer within highly ionizing environments such as Low Earth Orbit (LEO). In general, these experiments—conducted over a range of different temperatures and sample thicknesses—have documented the precedence for polyethylene to undergo hydrogen loss as a primary degradation pathway, leading to the formation of *trans*-olefines (–C═C–), as well as cross-linking between the macro-molecular chains. For example, FTIR spectroscopy has been used[28] to observe the formation of terminal vinyl (–CH═$CH_2$) groups resultant from the chain-scission process in the irradiation of PE samples with 13.6 MeV $O^+$ ions over a 8–290 K temperature range.

Due to the lack of systematic laboratory studies, the focus of the present study is to simulate the interaction of singly ionized oxygen atoms as present in planetary magnetospheres and in the Solar Wind with low temperature hydrocarbon ices (methane, ethane, ethylene) as well as polyethylene. As elucidated above, the hydrocarbon ices are ubiquitous in the outer Solar System; polyethylene, which has the same empirical formula as ethylene, is investigated not only for comparison with the ethylene monomer, but also because polyethylene is utilized as a polymeric material in spacecrafts exposed to the magnetospheric ions. We hope to answer questions that include: will oxygen species from the solar wind and magnetospheres react with saturated and unsaturated hydrocarbons to form oxygen-bearing molecules such as alcohols and aldehydes once implanted in a hydrocarbon surface? At what rate will oxygen ions degrade a polyethylene polymer on the surface of a spacecraft? Herein, we present a detailed experimental study on the processing of thin methane, ethane, ethylene, and polyethylene films with energetic 5 keV oxygen ions ($O^+$) at 10 K. By using on-line and *in situ* FTIR spectroscopy and quadrupole mass spectrometry (QMS) to determine qualitatively the irradiation products in the solid state and in the gas phase and quantitatively measure temporal abundance profiles from the column densities of newly formed radiolytic products, we hope to elucidate the specific reaction pathways and kinetics leading to product formation. The results of these experiments will also have important implications to the understanding of irradiation processes pertaining to low temperature planetary surfaces rich in hydrocarbons both in the context of astrophysical ices and aerospace design.

## 2. Experimental

The irradiation experiments were performed in a stainless steel chamber which was evacuated to ultrahigh vacuum (UHV) conditions ($8.0 \pm 0.5 \times 10^{-11}$ Torr). Within the chamber, a highly polished 31.75 × 31.75 mm silver substrate was attached to the cold head of a closed-cycle helium refrigerator (CTI-Cryogenics CP-1020), which cooled the substrate to a temperature of 10.3 ± 0.3 K—measured by a Lakeshore DT-470 silicon diode sensor. Here, pure ice samples were created by depositing methane (American Gas Group Grade 5.0), ethane (Advanced Gas Technologies Grade 5.0), and ethylene (Advanced Gas Technologies Grade 5.0) onto the cooled substrate. A gas delivery system and hydrocarbon gas base pressure of $1.5 \times 10^{-8}$ Torr was used for gas deposition, which over a 6 min condensation period produced ice samples of reproducible thicknesses (see below). During this procedure, the gases were monitored for contaminants using a Balzer QMG 420 QMS operating in residual gas analyzer mode (electron impact energy of 100 eV at a 0.3 mA emission current). Ice thickness verification was performed by a Nicolet 6700 FTIR recording the 6000–500 $cm^{-1}$ mid-infrared (mid-IR) spectrum of the samples. Each spectrum (resolution 2 $cm^{-1}$) is compiled from 196 individual scans collected over 2.0 min. Specific hydrocarbon absorption band intensities were then converted to molecular column densities (molecules $cm^{-2}$) by their integrated absorption coefficients (cm $molecule^{-1}$—Table 1) and thicknesses; the latter range from 75 ± 8 nm for ethylene to 138 ± 68 nm for methane (Table 1). These thicknesses (nm) were calculated *via* Bennett *et al.* (2006) using the low

**Table 1** Sample characterization of the irradiated targets

| Sample | Carrier | Position ($cm^{-1}$) | Absorption Coefficient (cm) | Thickness (nm) |
|---|---|---|---|---|
| $CH_4$ | $\nu_3 + \nu_4(CH_4)$ | 4328 | $(3.5 \pm 0.5) \times 10^{-19}$ [a] | 138 ± 68 |
| | $\nu_1 + \nu_4(CH_4)$ | 4220 | $(1.6 \pm 0.4) \times 10^{-19}$ [a] | |
| | $\nu_4(CH_4)$ | 1300 | $(6.2 \pm 0.6) \times 10^{-18}$ [a] | |
| $C_2H_6$ | $\nu_8(C_2H_6)$ | 1466 | $(2.7 \pm 0.3) \times 10^{-18}$ [a] | 88 ± 27 |
| | $\nu_9(C_2H_6)$ | 830 | $(1.9 \pm 0.2) \times 10^{-18}$ [a] | |
| $C_2H_4$ | $\nu_{11}(C_2H_6)$ | 2972 | $(1.0 \pm 0.2) \times 10^{-18}$ [b] | 75 ± 8 |
| | $\nu_7(C_2H_6)$ | 960 | $(1.5 \pm 0.3) \times 10^{-17}$ [b] | |
| HDPE | ··· | ··· | ··· | 130 ± 20 |

[a] Pearl *et al.* (1991). [b] Cowieson *et al.* (1981).

temperature densities (g $cm^{-3}$) of the hydrocarbons (Table 2). Samples of high density polyethylene (HDPE) were produced by spin coating a 2.0 wt% solution of HDPE (Goodfellow, $\rho$ = 0.94 g $cm^{-3}$, nominal size = 3 mm) dissolved in decalin (98%, Alfa Aesar) for 1 min (rotation speed of 2000 RPM) on a silver substrate and then annealed for 10 min at 403 K. Ellipsometry (Gaertner L116S) measurements of the samples, averaged at five positions on the substrate, determined that HDPE films were 130 ± 20 nm in thickness. These samples were directly attached to the cold head before the chamber was evacuated. Atomic Force Microscopy images of a representative HDPE sample are shown in Fig. 1.

The oxygen ions ($O^+$) were generated by a SPECS IQE 12/38 quadruply differentially pumped ion source fed with high purity oxygen gas ($O_2$: BOC Gases Grade 5.0) at a base pressure of $2.0 \times 10^{-4}$ Torr. A Wien mass filter located after the ionizing and extraction regions of the ion source was utilized to separate unwanted ions of $O_2^+$ and $O^{++}$; this setup resulted in a mono-energetic beam of 5 keV $O^+$ ions directed at the substrate (metastable ions could not be characterized within the ion beam and were considered as negligible at 5 keV acceleration energy). Before irradiation, the fluence of $O^+$ ions in the beam was optimized. These experimental settings were not altered as any adjustment of the optimized $O^+$ beam parameters resulted in an unstable ion current, prohibiting any fluence dependent experiments to be performed. A target mounted Faraday cup measured a total $O^+$ current of 10 ± 2 nA irradiating the 0.50 ± 0.06 $cm^2$ surface. A detailed description of the ion source and its calibration is provided in Ennis *et al.* (2011).[29] The hydrocarbon ices and the HDPE samples were then irradiated for 5 h isothermally at 10.3 ± 0.3 K. During this period, an on line analysis of the solid state was performed by FTIR spectroscopy, while the gas phase was monitored by the QMS. The on line gas phase analysis showed that no sputtering of the surface had occurred prior to the annealing stage where desorption of the solid matrices was performed. Upon the completion of the $O^+$ exposure period, the irradiated samples were left for a 20 min period before being annealed to 300 K at 0.5 K $min^{-1}$ by a 50 Ω heater attached to the cold head. This procedure enabled desorption of volatile species from the target under UHV conditions thus allowing for their identification in the gas phase *via* QMS.

Theoretically, the $O^+$ ion trajectories within the solids were simulated using the SRIM Monte Carlo program.[30] These calculations showed that the maximum stopping range for the impinging $O^+$ ions (Table 2) was always less than the sample thickness; this suggests that a complete transfer of the kinetic energy of the $O^+$ ion ($E_k$) to the sample was achieved in all experiments. Subsequently, the average *dose* (eV $molecule^{-1}$) absorbed by each molecule in the sample (monomer unit in the case of HDPE) could be calculated (Table 2).

**Table 2** Experimental parameters for the $O^+$ implantation experiments

| Sample | Density (g $cm^{-3}$) | Maximum penetration depth (nm) | Implanted oxygen ions ($\times 10^{15}$ atoms) | Total deposited energy ($\times 10^{19}$ eV) | Average dose ($\times 10^2$ eV $molecule^{-1}$) |
|---|---|---|---|---|---|
| $CH_4$ | 0.53 | 33 ± 2 | 3.7 ± 0.6 | 1.9 ± 0.3 | 5.7 ± 1.9 |
| $C_2H_6$ | 0.71 | 26 ± 1 | 3.4 ± 0.6 | 1.7 ± 0.3 | 9.1 ± 3.1 |
| $C_2H_4$ | 0.80 | 25 ± 1 | 1.3 ± 0.4 | 0.3 ± 0.1 | 1.6 ± 0.8 |
| HDPE | 0.93 | 21 ± 1 | 3.4 ± 0.6 | 1.7 ± 0.3 | 7.9 ± 2.7 |

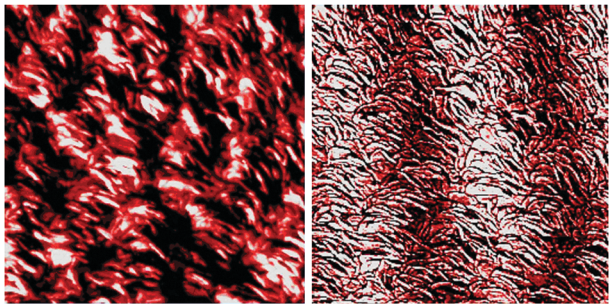

**Fig. 1** Atomic Force Microscope (AFM) image (4 × 4 $\mu m^2$) of a 130 ± 20 nm thick high-density polyethylene (HDPE) film on a silicon wafer showing lamellae structures.

## 3. Results

### 3.1 Infrared spectroscopy

**Methane.** Fig. 2(a) shows the 5500–600 $cm^{-1}$ mid-IR spectrum obtained from the pristine methane ice sample at 10 K. Also depicted is the spectrum collected immediately after the sample was irradiated with $O^+$ ions for 5 h at 10 K. Band positions and assignments pertaining to the solid methane infrared spectra are compiled in Table 3. In the pristine ice spectrum, the intense absorption band is assigned to the $\nu_4$ fundamental mode peaks at 1299 $cm^{-1}$. Spanning the 3009–3055 $cm^{-1}$ region is an intense absorption feature attributed to the $\nu_3$ C–H stretching fundamental. At higher frequencies (>4000 $cm^{-1}$), a number of combination bands (Table 3) can be identified, while at lower frequencies prominent overtone

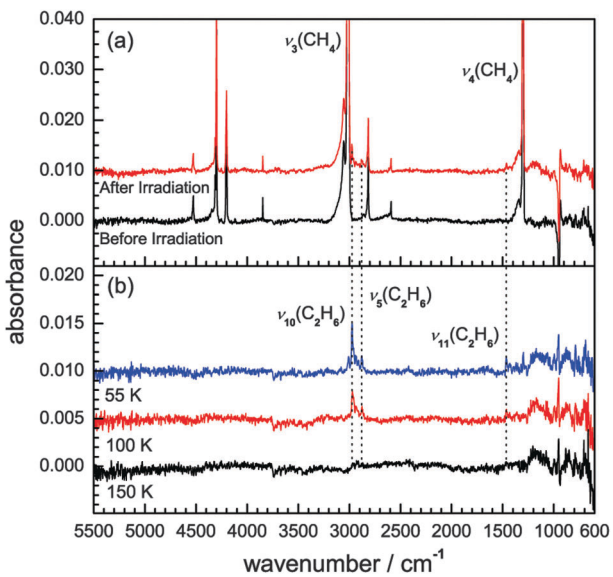


**Fig. 2** IR spectra of (a) pristine methane ice before and after $O^+$ irradiation at 10 K and (b) remaining absorption features at 55, 100, and 150 K during controlled heating of substrate. Absorption band positions and assignments are presented in Table 1.

 

**Table 3** Absorption band positions and assignments for irradiated methane ice from Fig. 2

| $CH_4$ Ice ($cm^{-1}$) | After irradiation at 11 K ($cm^{-1}$) | 100 K ($cm^{-1}$) | Assignment[a] | Characterization |
|---|---|---|---|---|
| 5794 | 5797 | ... | $\nu_1 + \nu_3(CH_4)$ | Combination |
| 5561 | 5562 | ... | $\nu_3 + 2\nu_4(CH_4)$ | Combination |
| 4528 | 4527 | ... | $\nu_2 + \nu_3(CH_4)$ | Combination |
| 4312, 4300 | 4312, 4300 | ... | $\nu_3 + \nu_4(CH_4)$ | Combination |
| 4201 | 4201 | ... | $\nu_1 + \nu_4(CH_4)$ | Combination |
| 4116 | 4117 | ... | $\nu_2 + 2\nu_4(CH_4)$ | Combination |
| 3847 | 3847 | ... | $3\nu_4(CH_4)$ | Overtone |
| 3055, 3020, 3009 | 3055, 3020, 3010 | ... | $\nu_3(CH_4)$ | Fundamental |
| ... | 2973, 2958, 2935 | 2970, 2955, 2935 | $\nu_{10}(C_2H_6)$[b] | Ethane |
| ... | 2881 | 2874 | $\nu_5(C_2H_6)$[b] | Ethane |
| 2815 | 2815 | ... | $\nu_2 + \nu_4(CH_4)$ | Combination |
| 2592 | 2592 | ... | $2\nu_4(CH_4)$ | Overtone |
| ... | 1463 | 1463 | $\nu_{11}(C_2H_6)$[b] | Ethane |
| 1343, 1306, 1299 | 1343, 1307, 1300 | ... | $\nu_4(CH_4)$ | Fundamental |

[a] Chapados & Cabana (1972), Baciocco *et al.* (1987), Calvani *et al.* (1992). [b] Wisnosky *et al.* (1983).

features are located at 3847 $cm^{-1}$ ($3\nu_4$) and 2592 $cm^{-1}$ ($2\nu_4$), together with the $\nu_2 + \nu_4$ combination band at 2815 $cm^{-1}$. All these absorption bands can be confidently assigned after direct comparison to previously published spectra on phase II methane ice at temperatures less than 20 K.[31–33] Following irradiation with $O^+$ ions, new absorption bands were observed to appear in regions associated with the stretching (~2800–3000 $cm^{-1}$) and deformation (~1460 $cm^{-1}$) modes of alkane hydrocarbons. In Fig. 2(b), these features of weak intensity are more easily observed in the mid-IR spectra collected during the controlled heating of the substrate at 55, 100, and 150 K, following the sublimation of the methane from the surface. Here, evidence of ethane ($C_2H_6$) ice on the substrate is provided by absorption features located at 1463 $cm^{-1}$ and in the 2874–2970 $cm^{-1}$ region. These absorptions can be assigned to the $\nu_{11}$(–$CH_2$) deformation fundamental and the higher frequency $\nu_{10}$ and $\nu_5$ C–H stretching fundamentals of solid ethane respectively, which coincide with low-temperature ethane absorption data in the literature.[34,35]

**Ethane.** Fig. 3(a) depicts the 5500–600 $cm^{-1}$ mid-IR region for pristine ethane ice at 10 K, both before and immediately after the sample was irradiated with $O^+$ ions for 5 h. Absorption band positions and assignments for ethane ice are provided in Table 4. For pure ethane ice, fundamental band positions are observed at 819 $cm^{-1}$ for the $\nu_{12}$ $CH_3$ rocking mode, at 1370 $cm^{-1}$ and 1464 $cm^{-1}$ for the $\nu_6$ and $\nu_{11}$ $CH_3$ deformation modes respectively, at 2879 $cm^{-1}$ for the $\nu_5$ CH symmetric stretching mode, and at 2970–2977 $cm^{-1}$ for the $\nu_{10}$ CH asymmetric stretching mode. In addition, there are a combination and overtone bands[36] located above 4000 $cm^{-1}$, the positions of which are summarized in Table 4. The assignment of these solid ethane absorption bands is in agreement with literature values previously obtained on solid ethane.[34] The spectra also suggests that the ethane ice is amorphous,[37] as the $\nu_{12}(CH_3)$ rocking band at 819 $cm^{-1}$ and the $\nu_{11}(CH_3)$ deformation band at 1464 $cm^{-1}$ both appear as single peaks (*i.e.* without splitting as seen in the crystalline phase at ~40 K). Only a small number of new absorption features are identified in the spectra collected after $O^+$ exposure (Fig. 3a). Solid methane[31] is identified as an irradiation product by its characteristic

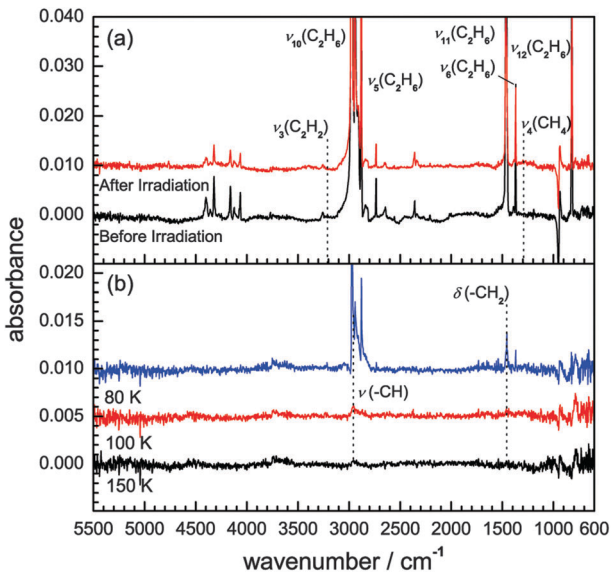


**Fig. 3** IR spectra of (a) pristine ethane ice before and after $O^+$ irradiation at 10 K and (b) remaining absorption features at 80, 100, and 150 K during controlled heating of substrate. Absorption band positions and assignments are presented in Table 2.

$\nu_4$ deformation and $\nu_3$ C–H stretching peaks located at 1300 $cm^{-1}$ and 3005 $cm^{-1}$ respectively. Acetylene ($C_2H_2$) is also characterized by its $\nu_3$ C–H stretching mode at 3238 $cm^{-1}$.[38] In Fig. 3(b), as the substrate was heated past the ethane sublimation temperature (60–70 K), the newly formed volatile molecules and reactive radical species are no longer evident in the spectra. Remaining at 80 K are a number of weak intensity absorption bands located in regions that overlap the original ethane fundamental modes; at ~2870–2970 $cm^{-1}$, 1460 $cm^{-1}$, and 1370 $cm^{-1}$. As ethane has sublimated from the surface by 80 K, these bands are most likely to be associated with higher-order hydrocarbons formed during the irradiation of the sample. Similar C–H stretching and –$CH_2$ deformation absorption signatures were identified from the irradiation of pure ethane and propane ices with 5 keV electrons,[5] inferring an aliphatic hydrocarbon residue—with some evidence of branched –$CH_3$ groups—remained on the substrate after heating to 300 K.

**Table 4** Absorption band positions and assignments for irradiated ethane ice from Fig. 3

| $C_2H_6$ ice ($cm^{-1}$) | After irradiation at 11 K ($cm^{-1}$) | 80 K ($cm^{-1}$) | Assignment[a] | Characterization |
|---|---|---|---|---|
| 4398, 4356, 4320, 4160, 4124, 4106, 4071, 4063 | 4397, 4356, 4319, 4159, 4124, 4063 | ··· | ··· | Combination and overtone bands |
| 3258 | 3254 | ··· | $\nu_4 + \nu_{10}(C_2H_6)$ | Combination |
| ··· | 3238 | ··· | $\nu_3(C_2H_2)$[c] | Acetylene |
| ··· | 3005 | | $\nu_3(CH_4)$[b] | Methane |
| 2977, 2970 | 2977, 2970 | 2971 | $\nu_{10}(C_2H_6)$ | Fundamental |
| 2956, 2941, 2907 | 2957, 2941, 2908 | 2940, 2911 | $\nu_8 + \nu_{11}(C_2H_6)$ | Combination |
| 2879 | 2880 | 2879 | $\nu_5(C_2H_6)$ | Fundamental |
| 2837, 2819 | 2838, 2820 | ··· | $\nu_6 + \nu_{11}(C_2H_6)$ | Combination |
| 2732 | 2735 | 2732 | $\nu_2 + \nu_6(C_2H_6)$ | Combination |
| 2644 | 2646 | ··· | $\nu_8 + \nu_{12}(C_2H_6)$ | Combination bands |
| 2557 | 2557 | ··· | ··· | |
| 2358, 2334 | 2359, 2335 | 2358, 2333 | ··· | |
| 2274 | 2274 | ··· | ··· | |
| 2207 | 2205 | ··· | ··· | |
| 2013, 2001 | 2010 | ··· | ··· | |
| 1749 | 1755 | ··· | ··· | |
| 1464 | 1464 | 1457 | $\nu_{11}(C_2H_6)$ | Fundamental |
| 1370 | 1369 | 1370 | $\nu_6(C_2H_6)$ | Fundamental |
| ··· | 1300 | ··· | $\nu_4(CH_4)$[b] | Methane |
| 819 | 819 | ··· | $\nu_{12}(C_2H_6)$ | Fundamental |

[a] Wisnosky *et al.* (1983), Hepp and Herman (1999). [b] Chapados & Cabana (1972). [c] Khanna *et al.* (1988).

**Ethylene.** The 5500–600 $cm^{-1}$ mid-IR spectrum for pristine ethylene ice at 10 K is presented in Fig. 4(a), together with the spectrum recorded immediately after the sample was irradiated with $O^+$ ions for 5 h. Table 5 compiles the absorption band positions and vibrational assignments for ethylene ice. Low frequency ethylene fundamental modes are observed at 821 $cm^{-1}$ for the $\nu_{10}$ $CH_2$ rocking mode, at 950 $cm^{-1}$ for the $\nu_8$ $CH_2$ wagging mode and at 1437 $cm^{-1}$ for the $\nu_{12}$ $CH_2$ deformation mode. At higher frequencies, the ethylene $\nu_{11}$ and $\nu_9$ C–H stretching modes are observed at 2972 $cm^{-1}$ and 3065–3087 $cm^{-1}$ respectively. The positions of these fundamental peaks correlate well with published data on crystalline ethylene ice.[39] In addition to the fundamental peaks of ethylene, combination and overtone bands are located from 1500 $cm^{-1}$ to 2500 $cm^{-1}$ and towards the near-IR region at frequencies higher than 4000 $cm^{-1}$ (Table 5). There are only a limited number of new absorption features that can be clearly identified in the spectra collected after $O^+$ exposure. Acetylene can be confirmed as an irradiation product by its distinctive $\nu_3$ C–H stretching frequency at 3236 $cm^{-1}$.[38] The remaining absorption features positioned from 2960–2870 $cm^{-1}$ and at 1458 $cm^{-1}$ can be confidently assigned to C–H stretching and $-CH_2$ deformation vibrations of hydrocarbons.[40] As the substrate is heated to 150 K, these features remain as relatively intense peaks in the mid-IR spectrum (Fig. 4b), indicating that higher-order aliphatic species are produced by ethylene irradiation over the irradiated methane and ethane condensates investigated earlier. The remaining peaks are therefore likely to be associated with the low frequency vibrational modes of higher-order hydrocarbons.

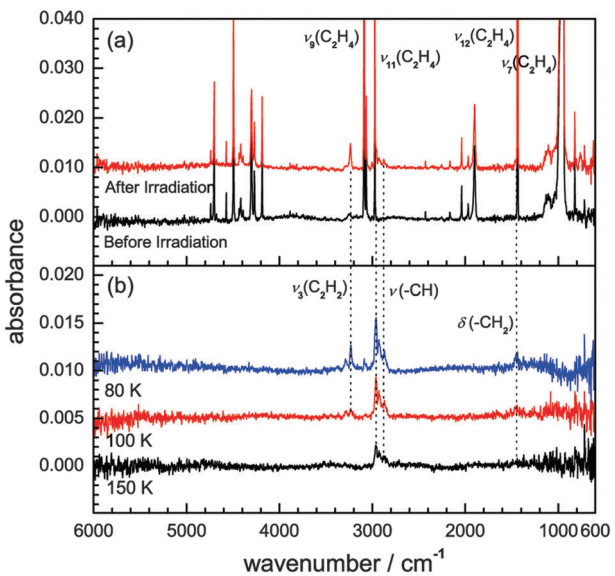


**Fig. 4** IR spectra of (a) pristine ethylene ice before and after $O^+$ irradiation at 10 K and (b) remaining absorption features at 80, 100, and 150 K during controlled heating of substrate. Absorption band positions and assignments are presented in Table 3.

**Polyethylene.** Fig. 5 shows 5500–600 $cm^{-1}$ mid-IR spectra for polyethylene spun coated on a polished silver substrate at (a) 10 K, (b) 100 K, and (c) 300 K—both before and immediately after irradiation with $O^+$ ions for 5 h. Absorption band positions and assignments for the polyethylene spectra are compiled in Table 6. The most intense absorption features are located at 2847 $cm^{-1}$ and at 2926–2913 $cm^{-1}$, pertaining to the respective $\nu_s$ symmetric and $\nu_a$ asymmetric stretching modes of the repeating $-(C_2H_4)-$ monomer unit. At 1474 $cm^{-1}$ and 1462 $cm^{-1}$, the absorption bands associated with the main chain $-CH_2-$ bending mode, $\delta(B_{1u}, B_{2u})$, can be observed, while at 1375 $cm^{-1}$ the corresponding bending vibration for the terminal $-CH_3$ group is located, displaying considerably less intensity. Low frequency polyethylene vibrational modes are positioned at 733 $cm^{-1}$ and 720 $cm^{-1}$ for the $\gamma_r(-CH_2-)$ rocking modes, at 1171 $cm^{-1}$ for $\gamma_w(-CH_2-)$ wagging mode, and at 1259 $cm^{-1}$ for the $\gamma_t(-CH_2-)$ twisting mode. The positions of these vibration modes adhere to previously published theoretical and experimental results for the polyethylene macromolecule.[41]

 

**Table 5** Absorption band positions and assignments for irradiated ethylene ice from Fig. 4

| $C_2H_4$ ice ($cm^{-1}$) | After irradiation at 11 K ($cm^{-1}$) | 80 K ($cm^{-1}$) | Assignment[a] | Characterization |
|---|---|---|---|---|
| 4739, 4702, 4677, 4573, 4493, 4433, 4414, 4391, 4300, 4270, 4185 | 4739, 4702, 4677, 4573, 4493, 4433, 4416, 4391, 4300, 4270, 4185 | ··· | ··· | Combination and overtone bands |
| ... | 3236 | ··· | $\nu_3(C_2H_2)$[b] | Acetylene |
| 3087 | 3087 | ··· | $\nu_9(C_2H_4)$ | Fundamental |
| 3065 | 3065 | ··· | | |
| 2972 | 2972 | ··· | $\nu_{11}(C_2H_4)$ | Fundamental |
| 2964 | 2964 | 2961 | $CH_3$ stretching[c] | $C_nH_{2n+2}$ |
| ··· | ··· | 2929 | | |
| ··· | 2878 | 2870 | | |
| 2429 | 2429 | ··· | $\nu_2 + \nu_{10}(C_2H_4)$ | Combination bands |
| 2254 | 2254 | ··· | $\nu_4 + \nu_6(C_2H_4)$ | |
| 2166 | 2166 | ··· | $\nu_3 + \nu_{10}(C_2H_4)$ | |
| 2038 | 2038 | ··· | $\nu_6 + \nu_{10}(C_2H_4)$ | |
| 1969 | 1969 | ··· | $\nu_4 + \nu_8(C_2H_4)$ | |
| 1899 | 1899 | ··· | $\nu_7 + \nu_8(C_2H_4)$ | |
| ··· | 1465-1457 | 1458 | $CH_2$ bending[c] | $C_nH_{2n+2}$ |
| 1439-1435 | 1439-1435 | ··· | $\nu_{12}(C_2H_4)$ | Fundamental |
| 958-943 | 958-943 | ··· | $\nu_7(C_2H_4)$ | Fundamental |
| 821 | 821 | ··· | $\nu_{10}(C_2H_4)$ | Fundamental |

[a] Brecher and Halford (1961). [b] Khanna *et al.* (1988). [c] Comeford & Gould (1960).

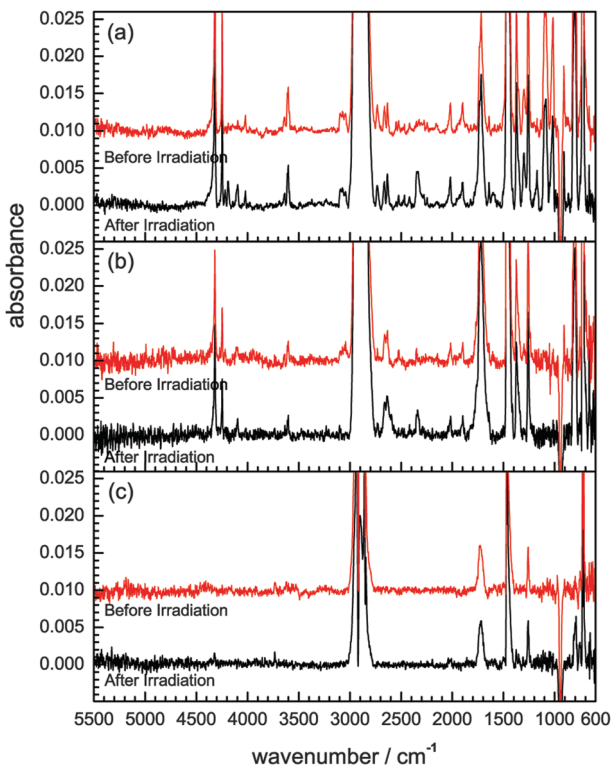


**Fig. 5** IR spectra of polyethylene film collected before and after $O^+$ irradiation at (a) 10 K, (b) 100 K, and (c) 300 K.

In addition to these absorption bands, low intensity combination and overtone bands are located from 1700 $cm^{-1}$ to 2050 $cm^{-1}$ and at frequencies higher than 3700 $cm^{-1}$ (Table 6). During the polyethylene exposure to $O^+$ ions at 10 K and 100 K (Fig. 5a and b), no new absorption feature are observed to increase in intensity over the irradiation period. Please note that the peak located at 2335 $cm^{-1}$, assigned to the $\nu_3$ asymmetric stretching vibration of carbon dioxide ($CO_2$) molecule, is observed to slightly fluctuate in intensity (corresponding to abundances of less than $1.0 \times 10^{15}$ molecules $cm^{-2}$) over the on-line analysis of the 10 K and 100 K samples. However, this is also observed in polyethylene samples not exposed to $O^+$ irradiation (blanks) suggesting that carbon dioxide is not a product of energetic particle exposure.

### 3.2 Mass spectrometry

Initially during the controlled heating of the 10 K samples, reactive species such as radicals that were previously trapped within the condensates are able to diffuse through the solid matrices more readily, which can further promote the formation of new molecules. In the case of the methane, ethane, and ethylene condensates, the gradual heating of the substrate also induces the sublimation of the respective ice matrices—and any molecular irradiation products—at their inherent sublimation temperatures. The gas phase analysis is performed using mass spectrometry, where sublimating molecules are collected and ionized by the QMS. Here, mass-to-charge ($m/z$) channels for the parent electron-impact ions of target molecules were pre-programmed and cyclically scanned during the annealing period. The detectable ion currents for selected species are presented in Fig. 6 as a function of substrate temperature (line format) and can be compared to the ion

**Table 6** Absorption band positions and assignments for irradiated polyethylene from Fig. 5

| PE ($cm^{-1}$) | After irradiation at 11 K | 100 K | 300 K | Assignment[a] | Characterization |
|---|---|---|---|---|---|
| 4319, 4246, 3853, 3743 | | | | ... | Combination and overtone bands |
| 2926, 2913 | | | | $\nu_a$ | $CH_2$ asym. stretch |
| 2847 | | | | $\nu_s$ | $CH_2$ sym. stretch |
| 2635 | | | | ... | Combination |
| ... | 2335 | 2335 | 2338 | $\nu_3(CO_2)$ | $CO_2$ asym. stretch |
| 2022 | 2016 | | | $\gamma_w + \gamma_r$ | Combination |
| 1901 | | | | $\gamma_r + \gamma_t$ | Combination |
| 1721 | | | | ... | Combination |
| 1474, 1462 | | | | $\delta(B_{1u}, B_{2u})$ | $CH_2$ bend |
| 1375 | | | | $\delta$ | $CH_3$ bend |
| 1259 | | | | $\gamma_t$ | $CH_2$ twist |
| 1171 | | | | $\gamma_w$ ($B_{3u}$) | $CH_2$ wag |
| 733, 720 | | | | $\gamma_r$ ($B_{1u}$, $B_{2u}$) | $CH_2$ rock |

[a] Krimm *et al.* (1956).

profiles collected from the blank ice samples (dotted format). Qualitative detection of a radiolytic product in the gas phase can only be confirmed if the ion current for the specific species is observed to increase from that of the non-irradiated blank sample.

**Methane.** Ion counts collected during the annealing of the irradiated methane ice sample are displayed in Fig. 6(a), where the sublimation of the methane ($CH_4^+$: $m/z = 16$) matrix is observed to occur at 35 K. The ion profile for molecular oxygen ($O_2^+$: $m/z = 32$) is observed to increase with the subliming condensate between 35 and 40 K, producing a higher ion current ($1 \times 10^{-10}$ A) than the non-irradiated blank sample. An abundance of hydrogen molecules ($H_2^+$: $m/z = 2$)—that did not diffuse from the condensate between

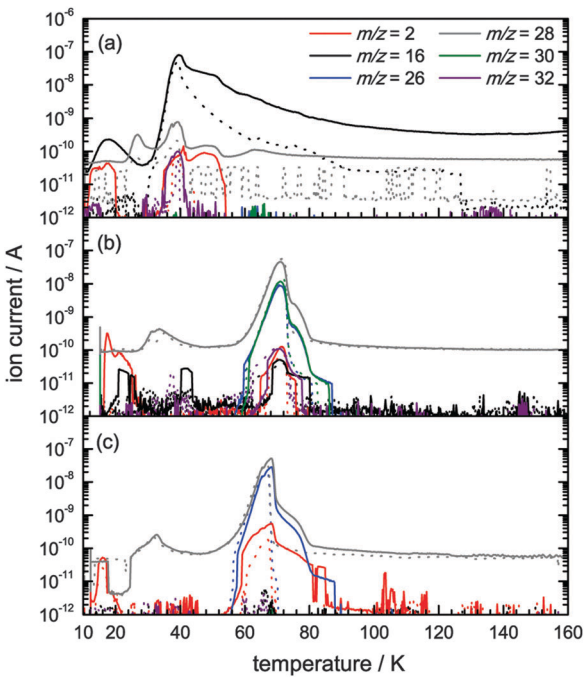


**Fig. 6** Ion counts for gas-phase species produced during the controlled heating of (a) methane ice, (b) ethane ice, and (c) ethylene ice; after irradiation with $O^+$ ions for five hours at 10 K. Ion counts for gas-phase species produced during the controlled heating of the pristine ice samples are depicted in dotted format.

10 and 20 K—is observed to sublime with the matrix at 40 K. Ion counts corresponding to ethane ($C_2H_6^+$: $m/z = 30$) appear between 60 and 70 K. Finally, between 130 and 140 K, an ion current for irradiation product methanol ($CH_3OH^+$: $m/z = 32$) is identified. As methanol and oxygen share the $m/z = 32$ channel, it is fortunate that methanol is retained on the substrate before subliming at a considerably high substrate temperature. The sublimation temperatures displayed in the present experiments correspond to those collected in previous studies involving the irradiation of methane and methanol under UHV conditions.[42] It can be stated that the higher sensitivity of the QMS instrument for gas phase species allows for the detection of an abundance of methanol which was not clearly identified by FTIR in the solid state (*i.e.* methanol's most intense feature $\nu_{11}(CH_3OH)$ at $\sim$1050 $cm^{-1}$ was not observed at 10 or 120 K).

**Ethane.** The sublimation of the irradiated and pristine ethane samples resulted in the ion profiles displayed in Fig. 6(b). The profile for the parent ethane ion channel ($C_2H_6^+$: $m/z = 30$) indicates that the condensates sublime between 60 and 80 K (peaking at $\sim$70 K), coinciding with previous experiments.[35] The overlaying ion currents for channels $m/z = 26$ ($C_2H_2$) and 28 ($C_2H_4$) show that they are not derived from irradiation products, but rather signals from electron impact fragments of the ethane molecule in the ionizer, $C_2H_2^+$ and $C_2H_4^+$ respectively. Therefore acetylene and ethylene, sharing similar sublimation temperatures to the ethane precursor, can not be identified by the QMS. The ion profile for molecular hydrogen ($H_2^+$: $m/z = 2$) shows the species is largely outgassed between 15 and 25 K, although some is released with the condensate. The channel for $m/z = 16$ appears to fluctuate in its ion current over the annealing period. The rise at 20–30 K is probably due to the high cross-section for oxygen molecules (traces of the $O_2^+$: $m/z = 32$ signal also evident at 20–30 K) to fragment and ionize to oxygen ions ($O^+$: $m/z = 16$) *via* electron impact.[43] However, between 35 and 50 K and during the sublimation of the condensate (60–80 K) the increase in the $m/z = 16$ ion current to $\sim 5 \times 10^{-11}$ A above the blank level can be attributed to irradiation product methane ($CH_4$). The formation of methanol ($CH_3OH$) can account for the $m/z = 32$ signal at 145 K ($\sim$5 K higher sublimation temperature than

 

the irradiated methanol profile in Fig. 6a), however, there was no observation of $m/z = 46$ signal above the detection limit of the QMS to suggest the presence of ethanol ($C_2H_5OH$) in the gas-phase.

**Ethylene.** The ion profiles collected from the annealed pristine and $O^+$ irradiated ethylene ice samples are presented in Fig. 6(c). Here, the ethylene matrix is observed to sublime at a substrate temperature between 55 and 75 K, as indicated by the species parent ($C_2H_4^+$: $m/z = 28$) ion current. Note this channel is shared with carbon monoxide ($CO^+$: $m/z = 28$), however, as carbon monoxide sublimes between 30 and 40 K, the two species can be distinguished in a qualitative sense. No increase in carbon monoxide over the blank experiment abundance was observed from the irradiated sample. The ion current recorded for $m/z = 26$ during the sublimation of the condensate is not derived from the irradiation product acetylene ($C_2H_2$) subliming at the same temperature as the ethylene precursor, but as $C_2H_2^+$ being formed with high yield by the fragmentation of ethylene in the residual gas ionizer. Molecular hydrogen ($H_2^+$: $m/z = 2$) is once again observed to be out-gassed shortly after the heating is initiated (10–15 K) and with the subliming matrix ($\sim$60 K). Only a trace signal for oxygen ($O_2^+$: $m/z = 32$) molecules is displayed over its expected sublimation range ($\sim$35–40 K), however, a slightly higher abundance is released to the gas phase with the condensate. Otherwise, no ion counts associated with molecular irradiation products were observed above the signal-to-noise threshold during the entire annealing period to 300 K.

Fig. 6 displays that for each of the methane, ethane, and ethylene experiments, the ion profiles for the parent ($CH_4^+$: $m/z = 16$, $C_2H_6^+$: $m/z = 30$, $C_2H_4^+$: $m/z = 28$ respectively) and main fragment ions in the irradiated experiment have extended 'tails' in comparison to the ion profiles recorded in the pristine experiments. This generally signifies that a residue has formed on the surface of the substrate over the course of irradiation, presumably forming higher order aliphatic hydrocarbons.[5] As polymerized hydrocarbons display sublimation temperatures above 300 K, they remain in the solid state and impede the release of the molecular composition of the condensate at its normal sublimation temperature. This effect is particularly evident in the irradiated methane experiment in Fig. 6(a), where out-gassing of methane from the surface is prolonged and continues at temperatures past 100 K.

**Polyethylene.** Finally, please note that mass spectrometry was additionally performed for the polyethylene samples, both during the irradiation period (10–300 K) and during the controlled heating of the low temperature samples to 300 K. The only species that could be identified above the signal-to-noise threshold ($1 \times 10^{-12}$ A) of the QMS was molecular hydrogen ($H_2$), evolved from the polyethylene samples irradiated at 100 and 300 K. In both cases, molecular hydrogen showed a small increase in ion current to $\sim 8 \times 10^{-11}$ A during the irradiation period, above its residual background abundance ($\sim 3 \times 10^{-11}$ A). There was no evidence for increased abundances of radiolytic carbon monoxide (CO) or carbon dioxide ($CO_2$) formed from the three samples above their constant background abundances of $\sim 8 \times 10^{-11}$ A and $\sim 5 \times 10^{-12}$ A respectively. Finally, there was no observed increase in the gas-phase abundance of molecular oxygen ($O_2$), either during the irradiation period or during the controlled heating of the low temperature polyethylene samples, to indicate the recombination of implanted oxygen ions. Ion profiles are not included for these experiments for simplicity.

## 4. Discussion

A qualitative analysis of the $O^+$ irradiated hydrocarbon ices and polyethylene samples has uncovered a host of molecular products, both in the solid-state by FTIR spectroscopy and in the gas phase by mass spectrometry. These species are compiled in Table 7, which shows that molecular hydrogen loss is a common degradation pattern during the processing of these hydrocarbons with fast oxygen ions. Herein the discussion, we provide details on the formation routes for all detected species, and propose reaction pathways with detailed kinetic analysis of the observed product abundances within the solid state.

### Methane

As observed in Fig. 2, absorption bands assigned to the $\nu_{10}$, $\nu_5$, and $\nu_{11}$ vibrational modes of solid ethane were the only new mid-IR features that could be identified from the irradiation of methane ice with $O^+$ ions. Note that previous studies[42] of methane ice (4 μm) exposed to energetic 7.3 MeV protons and 9.0 MeV α-particles at 10 K also identified ethane by FTIR spectroscopy in addition to acetylene, ethylene, and propane and a suite of reactive intermediates such as the methyl ($CH_3$), methylene ($CH_2$), ethyl ($C_2H_5$), and vinyl ($C_2H_3$) radicals.

The reaction of two neighboring methyl ($CH_3$) radicals presents a feasible reaction pathway for ethane formation in irradiated methane ices. Firstly, the methane molecule C–H bond can be ruptured by (1a) a direct collision with the impinging $O^+$ ion (or neutralized O atom) generating a knock on hydrogen atom or by (1b) interaction with a secondary electron ejected from the ion-track of the impinging $O^+$ ion through the target. The Gibbs free energy ($\Delta_R G$) required to break a methane C–H bond has been previously calculated to be 4.48 eV,[44] which can be transferred to the methane molecule *via* nuclear ($S_n$) or electronic ($S_e$) interaction from the impinging particle. Please note term symbols are omitted throughout this section for clarity and that these can be obtained from the included references).

$$CH_4 \xrightarrow{O^+/O} CH_3 + H \quad (1a)$$

$$CH_4 \xrightarrow{e^-} CH_3 + H \quad (1b)$$

Furthermore, a methyl radical may be formed by a hydrogen abstraction channel *via* (1c) reaction with a suprathermal oxygen

**Table 7** Summary of observed individual molecular products

| | Sample | | | |
|---|---|---|---|---|
| | $CH_4$ | $C_2H_6$ | $C_2H_4$ | $[C_2H_4]_n$ |
| FTIR | $C_2H_6$ | $CH_4$, $C_2H_2$ | $C_2H_2$ | ··· |
| QMS | $H_2$, $O_2$, $C_2H_6$, $CH_3OH$ | $H_2$, $O_2$, $CH_4$, $CH_3OH$ | $H_2$, $O_2$ | $H_2$ |

atom in the matrix in producing a hydroxyl radical or *via* (1d) reaction with a hydrogen atom in producing a hydrogen molecule. The latter reaction has previously been calculated to have a $\Delta_R G$ value of 0.003 eV, after overcoming a barrier ($\Delta E_b$) of 0.65 eV.[45]

$$CH_4 + O \rightarrow CH_3 + OH \quad (1c)$$

$$CH_4 + H \rightarrow CH_3 + H_2 \quad (1d)$$

These pathways are expected to reduce the abundance of methane in the condensate. The initial methane column density ($2.9 \pm 1.5 \times 10^{17}$ molecules cm$^{-2}$) did not decrease (outside a 15% data point error) over the irradiation period. Also, dependent on the reversibility of reactions (1a) and (1b), atomic hydrogen and methyl radical recombination reactions (2) could reform the methane precursor to account for the methane column density.

$$CH_3 + H \rightarrow CH_4 \quad (2)$$

$$H + H \rightarrow H_2 \quad (3)$$

Mobile hydrogen atoms can also undergo recombination reactions (3) to form molecular hydrogen ($H_2$—undetectable by FTIR spectroscopy) or diffuse from the target into the UHV chamber. It follows that an interacting pair of methyl radicals can react ($\Delta_R G = -3.34$ eV)[44] to form an internally excited ethane molecule (4). Once formed, the vibrationally excited ethane molecule can revert to the ground state *via* phonon interaction with the matrix.

$$[CH_3 \cdots CH_3] \rightarrow [C_2H_6]^* \rightarrow C_2H_6 \quad (4)$$

In Fig. 7 we trace the growth of three characteristic ethane absorption bands to obtain the ethane temporal column density over the five hour irradiation period. Here we use a modified Beer–Lambert expression[46] and integral absorption coefficients[47] of $1.1 \pm 0.2 \times 10^{-17}$ cm molecule$^{-1}$ for the $\nu_{10}(C_2H_6)$ asymmetric stretching mode centered at 2960 cm$^{-1}$, $2.9 \pm 0.3 \times 10^{-18}$ cm molecule$^{-1}$ for the $\nu_5(C_2H_6)$ symmetric stretching mode at 2875 cm$^{-1}$, and $2.6 \pm 0.04 \times 10^{-18}$ cm molecule$^{-1}$ for the $\nu_{11}(C_2H_6)$ deformation mode at 1463 cm$^{-1}$. Each fundamental band calculates a maximum ethane column density of $\sim 2 \times 10^{15}$ molecules cm$^{-2}$, between 5000 and 10 000 s of $O^+$ exposure. After this time period, the ethane abundance appears to decrease within the solid. This may indicate that the species is further converted to 'higher-order' hydrocarbon species.[5] With respect to the reaction kinetics,[48] we shall express molecular ethane as the reaction intermediate that is formed from the interaction of two adjacent methyl radicals, following a simplified first-order reaction (5a). Subsequently the ethane intermediate is converted to an unassigned higher-order hydrocarbon species *via* (5b).

$$[CH_3 \cdots CH_3] \xrightarrow{k_1} C_2H_6 \quad (5a)$$

$$C_2H_6 \xrightarrow{k_2} C_XH_Y \quad (Y \geq X > 2) \quad (5b)$$

By applying eqn (6) to the data, we can fit the observed ethane abundance, $[C_2H_6]_t$ (molecules cm$^{-2}$), over the exposure time, $t$(s), to a pseudo first-order kinetic model involving two steps (A → B → C); as we attempt to fit the data to the simplest reaction model (first-order) before reverting to more complex models (*e.g.* consecutive models) if the first-order model does not fit. Here, we define the initial abundance of interacting methyl radicals as (A: $[CH_3 \cdots CH_3]_0$ in molecules cm$^{-2}$). The methyl radicals then react to yield the reaction intermediate ethane, (B: $[C_2H_6]_t$). It follows that the ethane molecules undergo radiolytic conversion to form an unassigned hydrocarbon product (C: $[C_XH_Y]_t$) at reaction rate $k_2$.

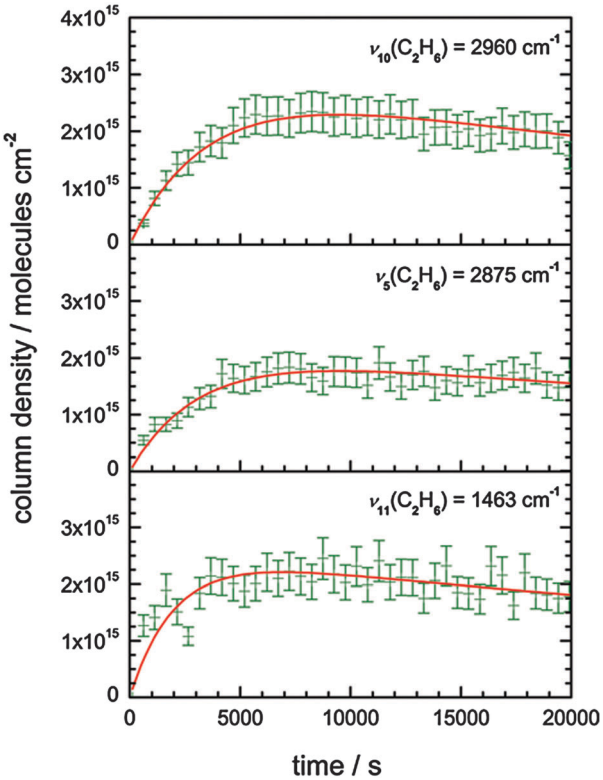


**Fig. 7** Temporal column densities (error of 15%) and fitted kinetic profiles for ethane formed during the irradiation of methane ice with $O^+$ ions.

$$[C_2H_6]_t = [CH_3 \cdots CH_3]_0 \frac{k_1}{k_2 - k_1}(e^{-k_1 t} - e^{-k_2 t}) \quad (6)$$

The fitted kinetic profiles for $[C_2H_6]_t$ are superimposed over the ethane temporal abundances for each vibration mode in Fig. 7. Here, the $[CH_3 \cdots CH_3]_0$ is calculated to be $2.4 \pm 0.4 \times 10^{15}$ molecules cm$^{-2}$, reacting to form ethane at an average reaction rate $k_1 = 3.4 \pm 1.1 \times 10^{-4}$ s$^{-1}$. Subsequently, the ethane abundance is depleted at an average rate $k_2 = 2.0 \pm 0.4 \times 10^{-4}$ s$^{-1}$ (Table 8). Furthermore, using eqn (7) and the kinetic parameters calculated from eqn (6), we derive an unassigned hydrocarbon product abundance, $[C_XH_Y]_t$, of $6.5 \pm 2.0 \times 10^{14}$ molecules cm$^{-2}$ at $t = 18\,000$ s.

$$[C_xH_y]_t = [CH_3 \cdots CH_3]_0 \left[1 - \frac{k_2}{k_2 - k_1} e^{-k_1 t} + \frac{k_1}{k_2 - k_1} e^{-k_2 t}\right] \quad (7)$$

### Ethane

The irradiation of solid ethane with $O^+$ ions resulted in new mid-IR absorption bands assigned to the $\nu_3$ and $\nu_4$ vibrational modes of solid methane and the $\nu_3$ vibrational

 

**Table 8** Kinetic data for proposed reaction pathways over all systems

| Pathway | Mode | $[A]_0$ (molecules cm$^{-2}$) | Rate Constants (s$^{-1}$) $k_1$ | $k_2$ |
|---|---|---|---|---|
| **Methane ice** | | | | |
| $[CH_3 \cdots CH_3] \xrightarrow{k_1} C_2H_6$ | $\nu_{10}(C_2H_6)$ | $2.9 \times 10^{15}$ | $2.8 \times 10^{-4}$ | $2.5 \times 10^{-5}$ |
| $C_2H_6 \xrightarrow{k_2} C_XH_Y$ $(Y \geq X > 2)$ | $\nu_{15}(C_2H_6)$ | $2.1 \times 10^{15}$ | $3.2 \times 10^{-4}$ | $1.8 \times 10^{-5}$ |
| | $\nu_{11}(C_2H_6)$ | $2.3 \times 10^{15}$ | $5.0 \times 10^{-4}$ | $1.8 \times 10^{-5}$ |
| | Ave. | $\mathbf{2.4 \pm 0.4 \times 10^{15}}$ | $\mathbf{3.4 \pm 1.1 \times 10^{-4}}$ | $\mathbf{2.0 \pm 0.4 \times 10^{-5}}$ |
| **Ethane ice** | | | | |
| $C_2H_6 \xrightarrow{k_1} CH_4 + CH_2$ | $\nu_4(CH_4)$ | $\mathbf{8.0 \pm 2.6 \times 10^{14}}$ | $\mathbf{k_1 = 3.1 \pm 1.2 \times 10^{-4}}$ | |
| $C_2H_6 \xrightarrow{k_1} C_2H_4 + H_2$ | $\nu_3(C_2H_2)$ | $\mathbf{2.1 \pm 0.5 \times 10^{14}}$ | $\mathbf{k_1 = 2.0 \pm 0.5 \times 10^{-3}}$ | |
| $C_2H_4 \xrightarrow{k_2} C_2H_2 + H_2$ | | | $\mathbf{k_2 = 3.2 \pm 1.0 \times 10^{-4}}$ | |
| **Ethylene ice** | | | | |
| $C_2H_4 \xrightarrow{k_1} C_2H_2 + H_2$ | $\nu_3(C_2H_2)$ | $\mathbf{7.3 \pm 1.4 \times 10^{14}}$ | $\mathbf{k_1 = 3.2 \pm 1.0 \times 10^{-4}}$ | |

mode of solid acetylene (Fig. 3). A similar qualitative study[49] of amorphous ethane (180 nm) ice irradiated with 30 keV $He^+$ ions at 12 K, also identified methane and acetylene as molecular products, in addition to ethylene. A subsequent study by the group,[50] pursuing the formation of polyynes from solid ethane *via* 200 keV $H^+$ bombardment ($\Phi \sim 5 \times 10^{14}$ ions cm$^{-2}$), detected ethylene and acetylene by Raman spectroscopy. A recent report[37] exposing amorphous (20 K), metastable (40 K), and crystalline (60 K) ethane ices with 0.8 MeV protons compiled the abundances of irradiation products methane, acetylene, ethylene, *n*-butane and $C_3H_x$ ($x$ = 4, 6, and 8) within the condensed ethane ices.

Regarding the present experiments, the most probable channel for methane formation involves the decomposition of the ethane precursor into a ground state methane molecule and a singlet methylene radical *via* retro-insertion (8). This pathway, initially proposed from the UV-photolysis of gas-phase ethane,[51] is calculated to be endoergic to a $\Delta_R G$ value of 4.32 eV after accounting for the differences in formation enthalpies of methane, ethane, and the methylene radical.[52] However, this energy can be supplied, for instance, by the impinging, energetic oxygen ion. The reaction involves a barrierless retro-insertion of singlet carbene ($CH_2$) into methane; this is analogous to the retro-insertion of an electronically excited oxygen atom into a C–H bond of methane for the unimolecular decomposition of methanol induced by fast electron irradiation performed previously in the group.[53] As observed previously for the temporal methane abundance, the ethane column density displayed no decrease over the irradiation period from its initial value of $1.5 \pm 0.2 \times 10^{17}$ molecules cm$^{-2}$. In addition, peaks pertaining to the methylene radical were not observed in the solid state at their calculated frequencies—although this might be expected due to their low calculated absorption coefficients.[53]

$$C_2H_6 \xrightarrow{k_1} CH_4 + CH_2 \qquad (8)$$

Fig. 8 shows the increase in methane abundance (molecules cm$^{-2}$) over the five hour exposure period. The temporal column densities for methane were calculated using an integral absorption coefficients of $6.2 \pm 0.6 \times 10^{-18}$ cm molecule$^{-1}$ for the $\nu_4(CH_4)$ deformation mode at 1300 cm$^{-1}$.[54] A maximum methane column density of $8.0 \pm 2.6 \times 10^{14}$ molecules cm$^{-2}$ was obtained at the completion of $O^+$ exposure (18 000 s). We now propose a simplified pseudo first-order kinetic model for the formation of methane *via* unimolecular decomposition of the ethane molecule (8). Using eqn (9), we fit the temporal abundance of the methane product, $[CH_4]_t$ (in molecules cm$^{-2}$), which is produced from an abundance of ethane precursor, $[C_2H_6]_0 = 8.0 \pm 2.6 \times 10^{14}$ molecules cm$^{-2}$, and is converted at a unimolecular reaction rate $k_1$ (s$^{-1}$) over the irradiation period, $t$. The fitted kinetic profile for $[CH_4]_t$ is superimposed over the methane temporal abundances in Fig. 8. We calculate the pseudo first-order reaction to proceed at a rate $k_1 = 3.1 \pm 1.2 \times 10^{-4}$ s$^{-1}$ (Table 8).

$$[CH_4]_t = [C_2H_6]_0 (1 - e^{-k_1 t}) \qquad (9)$$

Next we investigate the formation of molecular acetylene. Experimental evidence[44] suggests that acetylene can be produced—in the least number of reaction steps—by two

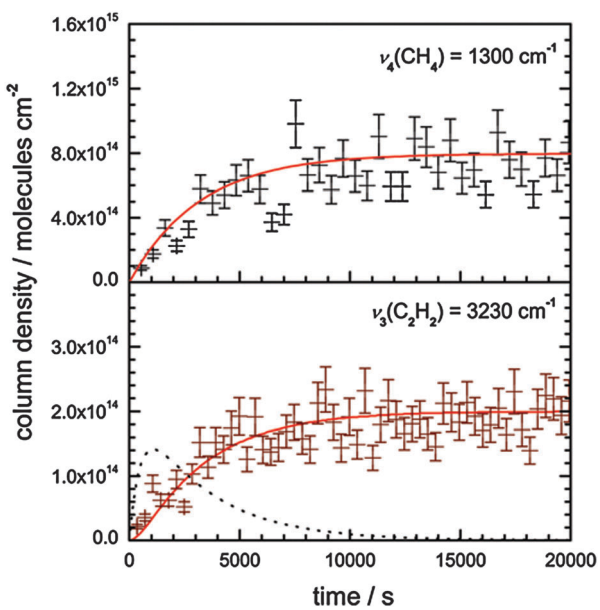


**Fig. 8** Temporal column densities (error of 15%) and fitted kinetic profiles for methane and acetylene formed during the irradiation of ethane ice with $O^+$ ions. The calculated ethylene temporal column density is superimposed on acetylene plot in dotted format.

successive molecular hydrogen elimination pathways *via* unimolecular decomposition of the ethane precursor and an ethylene intermediate (A → B → C). The initial reaction step in forming ethylene *via* molecular hydrogen elimination from ethane (10a) has been previously modeled for the electron irradiation of methane ice[44] and is calculated to proceed with a $\Delta_R G$ value of −1.37 eV after overcoming an entrance barrier of $\Delta E_b$ = 4.94 eV.[55] The subsequent step, the formation of acetylene from ethylene *via* molecular hydrogen elimination (10b), was also included in the irradiated methane scheme. Please note that for this reaction sequence, the unimolecular decomposition of the excited $[C_2H_6]^*$ molecular precursor and $[C_2H_4]^*$ intermediate presents a non-equilibrium and non-thermal processes in the low temperature ethane condensate. Precedence for analogous unimolecular decomposition pathways can be obtained from keV electron irradiation experiments in multiple hydrocarbon systems studied earlier in our group.[5,44,53,56]

$$[C_2H_6]^* \xrightarrow{k_1} [C_2H_4]^* + H_2 \quad (10a)$$

$$[C_2H_4]^* \xrightarrow{k_2} [C_2H_2]^* + H_2 \quad (10b)$$

Fig. 8 traces the abundance of the final product acetylene (C: $[C_2H_2]_t$ in molecules cm$^{-2}$) over the exposure period by applying an integral absorption coefficients of 3.2 ± 0.3 × $10^{-17}$ cm molecule$^{-1}$ [42] for its $\nu_3(C_2H_2)$ stretching mode located at 3230 cm$^{-1}$. The temporal abundance of acetylene, $[C_2H_2]_t$, formed from an ethane precursor (A: $[C_2H_6]_0$ = 2.0 ± 0.4 × $10^{14}$ molecules cm$^{-2}$), was then fitted by applying eqn (11) to the data.[48] Here, a maximum acetylene column density of 2.0 ± 0.4 × $10^{14}$ molecules cm$^{-2}$ was measured at 18 000 s—proceeding with successive reaction rates of $k_1$ = 2.0 ± 0.5 × $10^{-3}$ s$^{-1}$ and $k_2$ = 3.2 ± 1.0 × $10^{-4}$ s$^{-1}$ (Table 8).

$$[C_2H_2]_t = [C_2H_6]_0 \left[1 - \frac{k_2}{k_2 - k_1} e^{-k_1 t} + \frac{k_1}{k_2 - k_1} e^{-k_2 t}\right] \quad (11)$$

In addition, the temporal abundance of the ethylene intermediate (B: $[C_2H_2]_t$) can be derived from the kinetic data by applying eqn (12).[48] We calculate a maximum ethylene column density of 1.4 ± 0.4 × $10^{14}$ molecules cm$^{-2}$ at ∼1200 s—before its abundance tails away as $O^+$ irradiation continues. This abundance of ethylene molecules would yield a mid-IR absorption band of weak intensity (∼0.007 cm$^{-1}$) in the experimental spectra after applying an integrated absorption coefficient of 1.5 ± 0.3 × $10^{-17}$ cm molecules$^{-1}$ [57] for its most intense $\nu_7(C_2H_4)$ fundamental mode at ∼950 cm$^{-1}$. Even though this peak is positioned within an absorption free region of the irradiated ethane spectra, its predicted intensity is at the detection limit for the experimental FTIR setup and can not be confidently assigned above the signal-to-noise threshold.

$$[C_2H_4]_t = [C_2H_6]_0 \frac{k_1}{k_2 - k_1} (e^{-k_1 t} - e^{-k_2 t}) \quad (12)$$

## Ethylene

The mid-IR spectra of ethylene ice samples exposed to $O^+$ irradiation revealed the formation of solid acetylene, assigned by its $\nu_3$ vibrational mode at 3236 cm$^{-1}$ (Fig. 4). In addition, new infrared absorption bands were observed at positions associated with the –$CH_2$ bending mode (1458 cm$^{-1}$) and C–H stretching modes (2870 cm$^{-1}$, 2929 cm$^{-1}$, and 2961 cm$^{-1}$) of an aliphatic hydrocarbon species. As these peaks were observed at substrate temperatures exceeding 150 K during the annealing period, they are likely to be attributed to a higher-order hydrocarbon residue of general formula $C_XH_Y$ ($Y \geq X > 3$), formed by the irradiation induced polymerization of ethylene. Previous investigations[42] using on-line and *in situ* FTIR for the analysis of 10 K ethylene ice samples (∼5 μm) exposed to 7.3 MeV proton and 9.0 MeV α-particle irradiation identified primary radiolytic products ethane, acetylene, and the ethyl radical by their characteristic absorption bands. In addition, amorphous ethylene films (210 nm) were irradiated with 30 keV $He^+$ ions at 12 K,[49] which yielded solid methane, ethane, and acetylene while a subsequent study by the same group,[50] irradiating ethylene with 200 keV $H^+$ particles (Φ ∼ 5 × $10^{14}$ ions cm$^{-2}$), detected acetylene by Raman spectroscopy.

The formation of acetylene from ethylene is likely to follow a molecular hydrogen elimination pathway *via* unimolecular decomposition of an ethylene precursor (13). We can follow the temporal evolution of solid state acetylene in the ethylene condensate over the exposure period in Fig. 9. The acetylene column density (molecules cm$^{-2}$) was calculated using an integral absorption coefficients of 3.2 ± 0.3 × $10^{-17}$ for the $\nu_3(C_2H_2)$ stretching mode[42] where a maximum yield of 7.3 ± 1.4 × $10^{14}$ molecules cm$^{-2}$ was observed towards the end of the $O^+$ exposure (18,000 s). A simplified pseudo first-order reaction (13) is now proposed to model the reaction kinetics of acetylene formation using eqn (14). Here, we fit the temporal abundance of acetylene, $[C_2H_2]_t$ (in molecules cm$^{-2}$), formed from a starting abundance, $[C_2H_4]_0$, of 7.3 ± 1.4 × $10^{14}$ ethylene molecules cm$^{-2}$ at a unimolecular reaction rate $k_1$ (s$^{-1}$) over the irradiation period. It follows that the kinetic profile for $[C_2H_2]_t$ is fitted to the measured acetylene temporal abundances in Fig. 9. Here we calculate acetylene formation to proceed at a rate $k_1$ = 3.2 ± 1.0 × $10^{-4}$ s$^{-1}$ (Table 8). It can be noted that this reaction rate for the formation of acetylene from an irradiated ethylene is the same as from the excited ethylene intermediate as modeled for the sequential

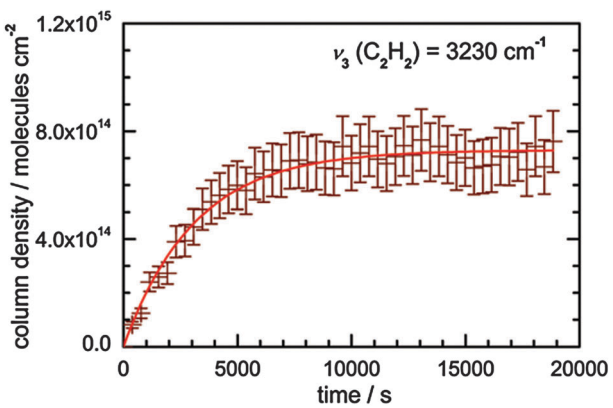


**Fig. 9** Temporal column density (error of 15%) and fitted kinetic profile for acetylene formed during the irradiation of ethylene ice with $O^+$ ions.

 

reaction pathway proposed above for the formation acetylene from oxygen ion irradiated ethane.

$$[C_2H_4]^* \xrightarrow{k_1} C_2H_2 + H_2 \quad (13)$$

$$[C_2H_2]_t = [C_2H_4]_0 (1 - e^{-k_1 t}) \quad (14)$$

### Polyethylene

There have been a number of laboratory studies (Summarized in Ennis & Kaiser (2010)[27]) involving the exposure of polyethylene (PE: $[C_2H_4]_n$) films with an array of energetic particles, primarily to test the degradation resistance of the polymer within highly ionizing environments such as Low Earth Orbit (LEO). In general, these experiments—conducted over a range of different temperatures and sample thicknesses—have documented the precedence for polyethylene to undergo hydrogen dissociation as a primary degradation pathway, leading to the formation of *trans*-vinylene (–C═C–) groups, as well as cross-linking between the macro-molecular chains. Previous studies[28] investigating the irradiation of PE samples with 13.6 MeV $O^+$ ions, over a 8–290 K temperature range, proposed chain scission as an alternate degradation pathway through their observation of vinyl (–CH═$CH_2$) end groups using FTIR spectroscopy.

For the present study, no new absorption bands pertaining to main-chain *trans*-vinylene (–C═C–) or vinyl (–CH═$CH_2$) end groups were observed to arise in the mid-IR spectra over the $O^+$ irradiation period at their expected positions; ~970 $cm^{-1}$ and ~1640 $cm^{-1}$ respectively. In addition, there was no spectroscopic evidence for the formation of carbonyl (C═O) groups at ~1720 $cm^{-1}$. The QMS data displayed only a small increase in the mass-to-charge profile for molecular hydrogen ($H_2$: $m/z$ = 2) for each of the three irradiation experiments at 10, 100, and 300 K. In addition there was no increase in gas phase abundance of carbon monoxide or carbon dioxide in any of the irradiated samples. Therefore, we must conclude that the irradiation of spin-coated polyethylene surfaces with 5 keV $O^+$ ions induces no detectable chemical modification to the detection limits of our solid state and gas-phase analysis.

### The fate of implanted oxygen

It is clear from the mid-IR analysis of $O^+$ irradiated hydrocarbons that oxygen-containing species are not readily detected in the solid state. However, the experimental irradiation conditions implanted a sufficient number of oxygen ions to yield a detectable abundance of oxygen-bearing molecules, even for reaction pathways occurring at low efficiency. For example, over the course of the five hour irradiation period of methane ice, the total $O^+$ ions supplied by the source (ion current of 10 ± 2 nA) was calculated to be $3.7 \pm 0.6 \times 10^{15}$ ions incident to the surface. Once the $O^+$ ion is neutralized and implanted into the surface, a singlet oxygen ($^1D$) atom can undergo insertion into a C–H bond of a target methane molecule to form methanol (15). This reaction is the reverse of the retro-insertion channel observed for the electron irradiation of solid methanol in producing methane and an excited oxygen atom.[58] Modeled to proceed at a rate $6.15 \times 10^{-6}$ $s^{-1}$, the retro-insertion of atomic oxygen was calculated to be slower than competing methanol destruction channels due to the need for the reaction to overcome a theoretical barrier energy of 5.86 eV.[59] Note that the methanol as detected in the ethane irradiation experiments could be also formed *via* reaction (15) since methane presents one of the reaction products in this system.

$$CH_4 + O \rightarrow CH_3OH \quad (15)$$

For the detection of solid-state methanol in the irradiated ices by FTIR, the most intense carrier of methanol is the $\nu_8(CH_3OH)$ C–O stretching fundamental, positioned at a vibrational frequency of ~1035 $cm^{-1}$. Using an integrated absorption coefficient of $1.3 \times 10^{-17}$ cm $molecule^{-1}$ for the $\nu_8(CH_3OH)$ mode,[60] $3.7 \pm 0.6 \times 10^{15}$ oxygen ions would produce an absorption peak of ~0.03 $cm^{-1}$ area, assuming that the formation channel for methanol *via* the insertion of an excited oxygen atom into a C–H bond of methane proceeds at a cross-section approaching unity as observed in gas-phase experiments of the system.[61–63] This calculated absorption peak area of 0.03 $cm^{-1}$ is difficult to detect above the baseline signal-to-noise in the mid-IR region (~0.01 $cm^{-1}$ peak area at frequencies higher than 1000 $cm^{-1}$).

However, the sublimation profiles obtained from the irradiated methane and ethane ices reveal that a small amount of methanol ($m/z$ = 32) is desorbed from the substrate between 140 and 150 K. The QMS instrument has high sensitivity for detection of trace molecular species in the condensate after subliming to the gas-phase. Unfortunately, direct quantitative calculation of the methanol gas-phase abundance could not be performed for the present experiments as the species $2.5 \pm 0.5 \times 10^{-12}$ A peak ion current (Fig. 6a and 6b) was near the threshold of the QMS detection limit. Perhaps the most likely fate for the $O^+$ ions implanted within the ice is to undergo neutralization to suprathermal oxygen atoms shortly after implantation in the solid. This would then allow for atomic oxygen neutrals to undergo radical-radical recombination reactions to form molecular oxygen (16).

$$O + O \rightarrow O_2 \quad (16)$$

The infrared inactivity of solid molecular oxygen prevents its observation in the predominantly hydrocarbon matrix using FTIR spectroscopy. Only trace quantities of $O_2$ produced from the recombination of atomic O species are speculated and not observed by FTIR. Often used to infer the presence of molecular oxygen in irradiated ice matrices with its intense stretching absorption feature, molecular ozone ($O_3$) was also not observed in the FTIR spectra; possibly due to strong hydrocarbon deformation bands interfering in its detection. In addition, mass signals attributed to the electron impact ionization of molecular oxygen ($O_2^+$: $m/z$ = 32) and its fragment ion ($O^+$: $m/z$ = 16) could not be detected in the gas-phase at the species of ~35 K sublimation temperature from the ethane and ethylene samples using the QMS (Fig. 6). However, a small abundance of oxygen could be identified subliming with the methane condensate, peaking at ~8 × $10^{-11}$ A. If the molecular oxygen reaction pathway is the most efficient within the experimental ices, we would expect a

maximum abundance of $1.8 \pm 0.6 \times 10^{15}$ oxygen molecules to be formed from the total number of oxygen ion implanted in the surface (column density of $3.7 \pm 0.6 \times 10^{15}$ molecules cm$^{-2}$). In comparison to the column density of methane making up the ice sample ($2.9 \pm 1.5 \times 10^{17}$ molecules cm$^{-2}$), this oxygen would represent a molecular ratio of $\sim$1 : 100 in the condensate after the exposure period.

### Comparison to electron irradiation experiments

Previous experiments[44] have simulated the energy transfer processes of MeV GCR particles impinging on Solar System hydrocarbon surfaces by using 5 keV electrons to irradiate 10 K methane ice surfaces. Quantitative analysis based on the destruction of the methane precursor and the observed abundances of radical intermediates ($CH_3$, $C_2H_5$, and $C_2H_3$) and molecular irradiation products ($C_2H_6$, $C_2H_4$, and $C_2H_2$) allowed for the development a complete reaction mechanism with associated rate constants. Furthermore, recent experiments[35] have used 5 keV electrons to irradiate ethane ices at 10, 30, and 50 K. Here, on-line FTIR spectroscopy measured the temporal abundances of molecular products methane, acetylene, ethylene, *n*-butane, and butene generated in the ice; leading to a comprehensive reaction mechanism being constructed for the electron irradiated ethane ices. As there have been no comparative studies irradiating ethylene ices with 5 keV electrons, the discussion of energetic interactions specific to this system has been omitted from this section.

From a purely qualitative perspective, the irradiation of methane and ethane ices with $O^+$ ions did not produce all of radiolytic products as observed in the mid-IR spectra as seen in the electron irradiation experiments (Table 9); particularly the presence of radical intermediates that might be important for the construction of complete reaction mechanisms. This could be due to the oxygen ions only penetrating the solid to a depth of $33 \pm 2$ nm for the methane ice and $26 \pm 1$ nm for the ethane ice (Table 2); corresponding to respective linear energy transfer (LET) values of $1.52 \pm 0.09 \times 10^5$ eV μm$^{-1}$ and $1.92 \pm 0.07 \times 10^5$ eV μm$^{-1}$. As the heavy oxygen ions come to rest, they predominantly transfer their kinetic energy to the matrix *via* nuclear ($S_n$) stopping interactions ($S_n/(S_n + S_e) = 0.74$)[30] which generate 'knock-on' particles by homolytic bond cleavage of the target molecules. This is opposed to the 5 keV electrons that are most likely to transmit through the $\sim$100 nm hydrocarbon ice layers, only depositing on average $\sim$350 eV per electron to the methane or ethane ice systems (LET = $3.5 \times 10^3$ eV μm$^{-1}$). Furthermore, electrons transfer their kinetic energy exclusively *via* electronic stopping interactions ($S_e$) which can initiate a cascade of secondary electrons borne with kinetic energies that are efficient for, for example, dissociative electron attachment and target bond dissociation.

Here, it is the comparable efficiency of 5 keV electrons to 5 keV oxygen ions in their ability to process a hydrocarbon surface which is of particular astrophysical interest (Table 9). Both electron irradiation studies irradiated the 10 K ices for a period of 1 h where the column densities calculated for the methane and ethane precursors were observed to decay by $\sim$6% and $\sim$20% respectively. This is opposed to no evident decay initiated by the oxygen ions for the methane and ethane samples from the present study within our error limits of 15%. It follows that the electron irradiation of methane yielded a total of $9.7 \pm 0.2 \times 10^{15}$ ethane molecules cm$^{-2}$, the most abundant irradiation product for the system, compared to the $2.4 \pm 0.4 \times 10^{15}$ ethane molecules cm$^{-2}$ yield from the oxygen ions over 5 h of exposure. We calculate that the $9.8 \pm 0.2$ ethane molecules generated per electron is a factor of 16 greater than the ethane yield per impinging $O^+$ ion. A similar trend is observed between the electron and $O^+$ irradiated ethane ice. Although the final abundances of methane ($1.5 \pm 0.2 \times 10^{15}$ molecules cm$^{-2}$) and acetylene ($4.0 \pm 2.0 \times 10^{14}$ molecules cm$^{-2}$) from the electron irradiated samples are of a similar magnitude to the $O^+$ irradiated samples ($8.0 \pm 2.6 \times 10^{14}$ methane molecules cm$^{-2}$ and $2.1 \pm 0.5 \times 10^{14}$ acetylene molecules cm$^{-2}$), the yield per electron is generally an order of magnitude higher than that obtained per $O^+$ ion. These results suggests that electronic stopping interactions play a more important role in initiating chemical modification of a hydrocarbon surface, as shown by the product yields obtained by fast electrons, compared to the nuclear stopping power (as important for implanted oxygen ions). Even though electronic interactions account for $\sim$26% of dissipated kinetic energy from the slowing $O^+$ ion, the cross-section of secondary electrons with energies sufficient for the breaking hydrocarbon C–H bonds ($\sim$5 eV) appears to be low.

## Conclusion

This paper focused on the processing of pure hydrocarbon ices (methane, ethane, ethylene) and polyethylene films by energetic (5 keV) oxygen ions—in order to determine the underlying principle reactions and product species formed as the impinging oxygen ions are implanted. The molecular products (summarized in Fig. 10) observed *via* FTIR spectroscopy are summarized by the following observations: (i) the irradiation of methane leads to ethane *via* the recombination of methyl radicals in a matrix cage, (ii) ethane can converted back to methane *via* a retro-insertion channel involving a methylene radical; further, ethane undergo unimolecular decomposition *via* ethylene forming acetylene, (iii) irradiated ethylene ices are converted to acetylene *via* hydrogen elimination. For (i) and (ii), when compared to 5 keV electron irradiation, the molecular yields induced by the oxygen ions is at least an order-of-magnitude less per particle, indicating that the nuclear ($S_n$) interactions may be less efficient in promoting chemical alteration of the hydrocarbon surface than electronic ($S_e$) interactions associated with relativistic electrons. As the $O^+$ ions impinge the solid, electronic stopping interactions generate a large number of highly ionizing secondary electrons before they are stopped; acting to accelerate the chemical processing of the hydrocarbon ice. No oxygen-containing species was observed in the solid-state. Therefore, it was likely that neutralized oxygen atoms recombined to form molecular oxygen within the condensate as detected *via* mass spectrometry. However, small abundances of gas-phase methanol were detected from the subliming methane and ethane condensates *via* mass spectrometry, indicating that oxygen insertion into methane may be an alternate reaction pathway in these systems. Placed in an astrophysical ice context, considering that methane,

 

**Table 9** Comparative molecular yields pertaining to electron and oxygen ion irradiation

| Molecular or radical species | 5 keV $e^-$ | | 5 keV $O^+$ | |
|---|---|---|---|---|
| | Δ Column density (molecules $cm^{-2}$) | Σ Molecules per electron | Δ Column density (molecules $cm^{-2}$) | Σ Molecules per oxygen ion |
| **Methane ice**[a] | | | | |
| $CH_4$ | $-1.2 \pm 0.2 \times 10^{16}$ | $-11.7 \pm 6.4$ | [c] | ... |
| $C_2H_6$ | $9.7 \pm 0.2 \times 10^{15}$ | $9.8 \pm 0.2$ | $2.4 \pm 0.4 \times 10^{15}$ | $0.6 \pm 0.2$ |
| Other ($CH_3$, $C_2H_5$, $C_2H_4$, $C_2H_3$, $C_2H_2$) | $5.2 \pm 0.4 \times 10^{15}$ | $5.3 \pm 0.4$ | Not observed | ... |
| **Ethane ice**[b] | | | | |
| $C_2H_6$ | $-2.4 \pm 0.7 \times 10^{16}$ | $-44 \pm 13$ | [c] | ... |
| $CH_4$ | $1.5 \pm 0.2 \times 10^{15}$ | $2.7 \pm 0.4$ | $0.8 \pm 0.3 \times 10^{15}$ | $0.2 \pm 0.1$ |
| $C_2H_2$ | $4.0 \pm 2.0 \times 10^{14}$ | $0.8 \pm 0.3$ | $2.1 \pm 0.5 \times 10^{14}$ | $0.06 \pm 0.02$ |
| Other ($C_2H_5$, $C_2H_4$, $C_4H_{10}$, $C_4H_8$) | $1.3 \pm 0.4 \times 10^{16}$ | $42 \pm 7$ | Not observed | ... |

[a] Bennett *et al.* (2006). [b] Kim *et al.* (2010). [c] Within experimental error limits (15%).

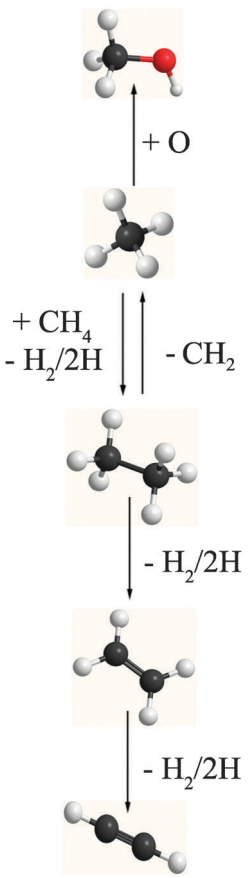


**Fig. 10** Reaction scheme depicting the chemical alteration of hydrocarbon ices *via* oxygen ion irradiation at 10 K.

ethane, and ethylene have been detected within the icy compositions of planetary moons and Trans-Neptunian objects, irradiation of oxygen ions in the present experiments ($\sim 5 \times 10^{11}$ oxygen ions $cm^{-2}$ $s^{-2}$) represents $\sim$50 000 years of processing a surface orbiting within the Saturnian magnetosphere ($\Phi \sim 1 \times 10^6$ $O^+$ $cm^{-2}$ $s^{-2}$ [23]) and much longer time periods on outer Solar System bodies where the $O^+$ flux is considerably lower as a component of the GCR radiation field. Here, the abundances of product molecules ($10^{14}$–$10^{15}$ molecules $cm^{-2}$), formed exclusively *via* $O^+$ irradiation, is a small fraction of their observed abundances when compared to the number densities generated by higher levels of photon and light particle ($H^+$, $He^+$, and $e^-$) irradiation. Finally, there was no significant alteration of the high density polyethylene samples to a detectable level due to $O^+$ exposure. As this is inconsistent with previous findings that have identified chain scission, cross-linking, and hydrogen elimination as prominent degradation mechanisms for polyethylene exposed to more energetic heavy nuclei exposure, the flux of $O^+$ provided in the present experiments is insufficient to generate observable levels of chemical alteration.

## Acknowledgements

It is with pleasure that CPE and RIK thank the Air Force Office of Scientific Research for support under Grant A9550-09-1-0177, while HY and SJS also acknowledge support from the AFOSR under Grant FA9550-10-1-0219. The operation of the charged particle source was supported by the W. M. Keck Foundation.

## References

1 I. C. F. Mueller-Wodarg, D. F. Strobel, J. I. Moses, J. H. Waite, J. Crovisier, R. V. Yelle, S. W. Bougher and R. G. Roble, *Space Sci. Rev.*, 2008, **139**, 191–234.
2 J. B. Dalton, D. P. Cruikshank, K. Stephan, T. B. McCord, A. Coustenis, R. W. Carlson and A. Coradini, *Space Sci. Rev.*, 2010, **153**, 113–154.
3 E. R. Stofan, C. Elachi, J. I. Lunine, R. D. Lorenz, B. Stiles, K. L. Mitchell, S. Ostro, L. Soderblom, C. Wood, H. Zebker, S. Wall, M. Janssen, R. Kirk, R. Lopes, F. Paganelli, J. Radebaugh, L. Wye, Y. Anderson, M. Allison, R. Boehmer, P. Callahan, P. Encrenaz, E. Flamini, G. Francescetti, Y. Gim, G. Hamilton, S. Hensley, W. T. K. Johnson, K. Kelleher, D. Muhleman, P. Paillou, G. Picardi, F. Posa, L. Roth, R. Seu, S. Shaffer, S. Vetrella and R. West, *Nature*, 2007, **445**, 61–64.
4 R. Courtin, *Space Sci. Rev.*, 2005, **116**, 185–199.
5 R. I. Kaiser, P. Maksyutenko, C. Ennis, F. Zhang, X. Gu, S. P. Krishtal, A. M. Mebel, O. Kostko and M. Ahmed, *Faraday Discuss.*, 2010, **147**, 429–478.
6 J. H. Waite, Jr., M. R. Combi, W. H. Ip, T. E. Cravens, R. L. McNutt, Jr., W. Kasprzak, R. Yelle, J. Luhmann, H. Niemann, D. Gell, B. Magee, G. Fletcher, J. Lunine and W. L. Tseng, *Science*, 2006, **311**, 1419–1422.
7 E. Quirico, S. Doute, B. Schmitt, C. de Bergh, D. P. Cruikshank, T. C. Owen, T. R. Geballe and T. L. Roush, *Icarus*, 1999, **139**, 159–178.
8 T. C. Owen, T. L. Roush, D. P. Cruikshank, J. L. Elliot, L. A. Young, C. de Bergh, B. Schmitt, T. R. Geballe, R. H. Brown and M. J. Bartholomew, *Science*, 1993, **261**, 745–748.

9 S. Doute, B. Schmitt, E. Quirico, T. C. Owen, D. P. Cruikshank, C. de Bergh, T. R. Geballe and T. L. Roush, *Icarus*, 1999, **142**, 421–444.
10 E. L. Schaller and M. E. Brown, *Astrophys. J.*, 2007, **670**, L49–L51.
11 M. E. Brown, K. M. Barkume, G. A. Blake, E. L. Schaller, D. L. Rabinowitz, H. G. Roe and C. A. Trujili, *Astron. J.*, 2007, **133**, 284–289.
12 L. M. Lara, W. H. Ip and R. Rodrigo, *Icarus*, 1997, **130**, 16–35.
13 V. A. Krasnopolsky and D. P. Cruikshank, *J. Geophys. Res.*, 1995, **100**, 21271–21286.
14 M. J. Mumma, M. A. DiSanti, N. Dello Russo, M. Fomenkova, K. Magee-Sauer, C. D. Kaminski and D. X. Xie, *Science*, 1996, **272**, 1310–1314.
15 T. Y. Brooke, A. T. Tokunaga, H. A. Weaver, J. Crovisier, D. Bockelee-Morvan and D. Crisp, *Nature*, 1996, **383**, 606–607.
16 H. A. Weaver, T. Y. Brooke, G. Chin, S. J. Kim, D. Bockelee-Morvan and J. K. Davies, *Earth, Moon, Planets*, 1997, **78**, 71–80.
17 R. E. Johnson, *Energetic Charged-Particle Interactions with Atmospheres and Surfaces*, Springer-Verlag, Berlin, 1990.
18 J. F. Cooper, E. R. Christian and R. E. Johnson, *Adv. Space Res.*, 1998, **21**, 1611–1614.
19 R. E. Johnson, *Rev. Mod. Phys.*, 1996, **68**, 305–312.
20 W. Zheng, D. Jewitt and R. I. Kaiser, *Astrophys. J.*, 2006, **648**, 753–761.
21 T. Cassidy, P. Coll, F. Raulin, R. W. Carlson, R. E. Johnson, M. J. Loeffler, K. P. Hand and R. A. Baragiola, *Space Sci. Rev.*, 2010, **153**, 299–315.
22 H. Melin, D. E. Shemansky and X. Liu, *Planet. Space Sci.*, 2009, **57**, 1743–1753.
23 E. C. Sittler Jr, A. Ali, J. F. Cooper, R. E. Hartle, R. E. Johnson, A. J. Coates and D. T. Young, *Planet. Space Sci.*, 2009, **57**, 1547–1557.
24 O. Gomis, M. A. Satorre, G. Strazzulla and G. Leto, *Planet. Space Sci.*, 2004, **52**, 371–378.
25 G. Strazzulla, J. R. Brucato, M. E. Palumbo and M. A. Satorre, *Nucl. Instrum. Methods Phys. Res., Sect. B*, 1996, **116**, 289–293.
26 M. E. Palumbo, *Adv. Space Res.*, 1997, **20**, 1637–1645.
27 C. P. Ennis and R. I. Kaiser, *Phys. Chem. Chem. Phys.*, 2010, **12**, 14884–14901.
28 M. Melot, Y. Ngono-Ravache and E. Balanzat, *Nucl. Instrum. Methods Phys. Res., Sect. B*, 2003, **209**, 205–211.
29 C. P. Ennis, C. J. Bennett and R. I. Kaiser, *Phys. Chem. Chem. Phys.*, 2011, **13**, 9469, DOI: 10.1039/C1CP20434C.
30 J. F. Ziegler, M. D. Ziegler and J. P. Biersack, Annapolis, SRIM-2008.04 edn, 2008.
31 C. Chapados and A. Cabana, *Can. J. Chem.*, 1972, **50**, 3521–3533.
32 G. Baciocco, P. Calvani and S. Cunsolo, *J. Chem. Phys.*, 1987, **87**, 1913–1916.
33 P. Calvani, S. Cunsolo, S. Lupi and A. Nucara, *J. Chem. Phys.*, 1992, **96**, 7372–7379.
34 M. G. Wisnosky, D. F. Eggers, L. R. Fredrickson and J. C. Decius, *J. Chem. Phys.*, 1983, **79**, 3505–3512.
35 Y. S. Kim, C. J. Bennett, L. H. Chen, K. O'Brien and R. I. Kaiser, *Astrophys. J.*, 2010, **711**, 744–756.
36 M. Hepp and M. Herman, *J. Mol. Spectrosc.*, 1999, **197**, 56–63.
37 R. L. Hudson, M. H. Moore and L. L. Raines, *Icarus*, 2009, **203**, 677–680.
38 R. K. Khanna, M. J. Ospina and G. Zhao, *Icarus*, 1988, **73**, 527–535.
39 C. Brecher and R. S. Halford, *J. Chem. Phys.*, 1961, **35**, 1109–1117.
40 J. J. Comeford and J. H. Gould, *J. Mol. Spectrosc.*, 1961, **5**, 474–481.
41 S. Krimm, C. Y. Liang and G. B. B. M. Sutherland, *J. Chem. Phys.*, 1956, **25**, 549–562.
42 R. I. Kaiser and K. Roessler, *Astrophys. J.*, 1998, **503**, 959–975.
43 P. C. Cosby, *J. Chem. Phys.*, 1993, **98**, 9560–9569.
44 C. J. Bennett, C. S. Jamieson, Y. Osamura and R. I. Kaiser, *Astrophys. J.*, 2006, **653**, 792–811.
45 T. Wu, H. J. Werner and U. Manthe, *Science*, 2004, **306**, 2227–2229.
46 C. J. Bennett, C. Jamieson, A. M. Mebel and R. I. Kaiser, *Phys. Chem. Chem. Phys.*, 2004, **6**, 735–746.
47 R. B. Bohn, S. A. Sandford, L. J. Allamandola and D. P. Cruikshank, *Icarus*, 1994, **111**, 151–173.
48 J. I. Steinfeld, J. S. Francasco and W. L. Hase, *Chemical Kinetics and Dynamics*, Prentice-Hall, New Jersey, 1989.
49 G. Strazzulla, G. A. Baratta, M. Domingo and M. A. Satorre, *Nucl. Instrum. Methods Phys. Res., Sect. B*, 2002, **191**, 714–717.
50 G. Compagnini, L. D'Urso, O. Puglisi, G. A. Baratta and G. Strazzulla, *Carbon*, 2009, **47**, 1605–1607.
51 H. Okabe and J. R. McNesby, *J. Chem. Phys.*, 1961, **34**, 668–669.
52 A. M. Mebel, S.-H. Lin and C.-H. Chang, *J. Chem. Phys.*, 1997, **106**, 2612–2620.
53 C. J. Bennett, S.-H. Chen, B.-J. Sun, A. H. H. Chang and R. I. Kaiser, *Astrophys. J.*, 2007, **660**, 1588–1608.
54 J. Pearl, M. Ngoh, M. Ospina and R. Khanna, *J. Geophys. Res.*, 1991, **96**, 17477–17482.
55 S. Irle and K. Morokuma, *J. Chem. Phys.*, 2000, **113**, 6139–6148.
56 Y. S. Kim, C. J. Bennett, L.-H. Chen, K. O'Brien and R. I. Kaiser, *Astrophys. J.*, 2010, **711**, 744–756.
57 D. R. Cowieson, A. J. Barnes and W. J. Orville-Thomas, *J. Raman Spectrosc.*, 1981, **10**, 224–226.
58 C. J. Bennett and R. I. Kaiser, *Astrophys. J.*, 2007, **661**, 899–909.
59 A. H. H. Chang and S. H. Lin, *Chem. Phys. Lett.*, 2004, **384**, 229–235.
60 M. E. Palumbo, A. C. Castorina and G. Strazzulla, *Astron. Astrophys.*, 1999, **342**, 551–562.
61 P. Casavecchia, R. J. Buss, S. J. Sibener and Y. T. Lee, *J. Chem. Phys.*, 1980, **73**, 6351–6352.
62 S. Satyapal, J. Park, R. Bersohn and B. Katz, *J. Chem. Phys.*, 1989, **91**, 6873–6879.
63 W. Hack and H. Thiesemann, *J. Phys. Chem.*, 1995, **99**, 17364–17371.